This paper is published as part of a PCCP Themed Issue on:

Physical chemistry of solids – the science behind materials engineering

Guest Editors: Jürgen Janek, Manfred Martin and Klaus Dieter Becker

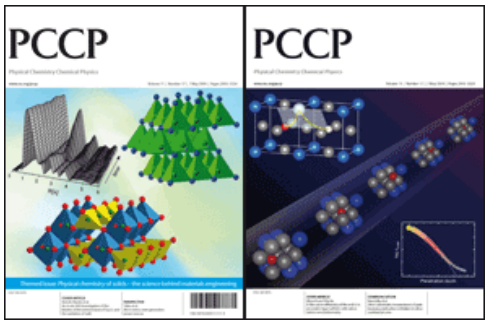

Editorial

Physical chemistry of solids—the science behind materials engineering
Phys. Chem. Chem. Phys., 2009
DOI: 10.1039/b905911n

Perspectives

Nanoionics: ionic charge carriers in small systems
Joachim Maier, *Phys. Chem. Chem. Phys.*, 2009
DOI: 10.1039/b902586n

Micro-ionics: next generation power sources
Harry L. Tuller, Scott J. Litzelman and WooChul Jung, *Phys. Chem. Chem. Phys.*, 2009
DOI: 10.1039/b901906e

Communications

On the conduction pathway for protons in nanocrystalline yttria-stabilized zirconia
Sangtae Kim, Hugo J. Avila-Paredes, Shizhong Wang, Chien-Ting Chen, Roger A. De Souza, Manfred Martin and Zuhair A. Munir, *Phys. Chem. Chem. Phys.*, 2009
DOI: 10.1039/b901623f

Direct calorimetric measurement of grain boundary and surface enthalpies in yttria-stabilized zirconia
Shushu Chen, Hugo J. Avila-Paredes, Sangtae Kim, Jinfeng Zhao, Zuhair A. Munir and Alexandra Navrotsky, *Phys. Chem. Chem. Phys.*, 2009
DOI: 10.1039/b819740g

Papers

Elastic strain at interfaces and its influence on ionic conductivity in nanoscaled solid electrolyte thin films—theoretical considerations and experimental studies
N. Schichtel, C. Korte, D. Hesse and J. Janek, *Phys. Chem. Chem. Phys.*, 2009
DOI: 10.1039/b900148d

Chemical and electronic properties of the ITO/Al_2O_3 interface
Yvonne Gassenbauer, André Wachau and Andreas Klein, *Phys. Chem. Chem. Phys.*, 2009
DOI: 10.1039/b822848e

Electronic state of oxygen nonstoichiometric $La_{2-x}Sr_xNiO_{4+\delta}$ at high temperatures
Takashi Nakamura, Keiji Yashiro, Kazuhisa Sato and Junichiro Mizusaki, *Phys. Chem. Chem. Phys.*, 2009
DOI: 10.1039/b823364k

B-Site cation diffusivity of Mn and Cr in perovskite-type $LaMnO_3$ with cation-deficit nonstoichiometry
Shogo Miyoshi and Manfred Martin, *Phys. Chem. Chem. Phys.*, 2009
DOI: 10.1039/b901208g

High anion conductivity in a ternary non-equilibrium phase of BaF_2 and CaF_2 with mixed cations
B. Ruprecht, M. Wilkening, A. Feldhoff, S. Steuernagel and P. Heitjans, *Phys. Chem. Chem. Phys.*, 2009
DOI: 10.1039/b901293a

Electrical and optical characterization of undoped $BaTiO_3$ in the quenched state
K.-D. Becker, M. Schrader, H.-S. Kwon and H.-I. Yoo, *Phys. Chem. Chem. Phys.*, 2009
DOI: 10.1039/b823174e

Oxidation states of Co and Fe in $Ba_{1-x}Sr_xCo_{1-y}Fe_yO_{3-\delta}$ (x, y = 0.2–0.8) and oxygen desorption in the temperature range 300–1273 K
Ashley S. Harvey, F. Jochen Litterst, Zhen Yang, Jennifer L. M. Rupp, Anna Infortuna and Ludwig J. Gauckler, *Phys. Chem. Chem. Phys.*, 2009
DOI: 10.1039/b819414a

Bulk defect chemistry and surface electronic behavior of Zn,Sn codoped In_2O_3 transparent conducting oxides
Steven P. Harvey, Thomas O. Mason, Christoph Körber and Andreas Klein, *Phys. Chem. Chem. Phys.*, 2009
DOI: 10.1039/b822149a

Defect chemistry of the cage compound, $Ca_{12}Al_{14}O_{33-\delta}$—understanding the route from a solid electrolyte to a semiconductor and electride
Doh-Kwon Lee, Lutz Kogel, Stefan G. Ebbinghaus, Ilia Valov, Hans-Dieter Wiemhoefer, Martin Lerch and Juergen Janek, *Phys. Chem. Chem. Phys.*, 2009
DOI: 10.1039/b818474g

Electrical conductivity–defect structure correlation of variable-valence and fixed-valence acceptor-doped $BaTiO_3$ in quenched state
Han-Ill Yoo, Tae-Sik Oh, Hyung-Soon Kwon, Dong-Kyu Shin and Jong-Sook Lee, *Phys. Chem. Chem. Phys.*, 2009
DOI: 10.1039/b822381p

An *in situ* XAS investigation of the kinetics of the ammonolysis of Ga_2O_3 and the oxidation of GaN
J. Brendt, D. Samuelis, T. E. Weirich and M. Martin, *Phys. Chem. Chem. Phys.*, 2009
DOI: 10.1039/b901819k

***In situ* investigation of coloration processes in $LiNbO_3$: MgO during reducing/oxidizing high-temperature treatments**
Dmytro Sugak, Yaroslav Zhydachevskii, Yuriy Sugak, Oleg Buryy, Sergii Ubizskii, Ivan Solskii, Alexander Börger and Klaus-Dieter Becker, *Phys. Chem. Chem. Phys.*, 2009
DOI: 10.1039/b822631h

Voltage-assisted ^{18}O tracer incorporation into oxides for obtaining shallow diffusion profiles and for measuring ionic transference numbers: basic considerations
J. Fleig, *Phys. Chem. Chem. Phys.*, 2009
DOI: 10.1039/b822415c

Oxygen incorporation into strontium titanate single crystals from CO_2 dissociation
Chr. Argirusis, F. Voigts, P. Datta, J. Grosse-Brauckmann and W. Maus-Friedrichs, *Phys. Chem. Chem. Phys.*, 2009
DOI: 10.1039/b901401b

Nearly constant loss effects in borate glasses
David M. Laughman, Radha D. Banhatti and Klaus Funke, *Phys. Chem. Chem. Phys.*, 2009
DOI: 10.1039/b822561n**Switching behaviour of modulated ferroelectrics I: kinetics of the field-induced lock-in transition of Rb_2ZnCl_4**
K. Elisbihani, H. Gibhardt and G. Eckold, *Phys. Chem. Chem. Phys.*, 2009
DOI: 10.1039/b902368b

Construction of nano- and microporous frameworks from octahedral bubble clusters
S. M. Woodley, M. B. Watkins, A. A. Sokol, S. A. Shevlin and C. R. A. Catlow, *Phys. Chem. Chem. Phys.*, 2009
DOI: 10.1039/b902600b

Bubbles and microporous frameworks of silicon carbide
M. B. Watkins, S. A. Shevlin, A. A. Sokol, B. Slater, C. R. A. Catlow and S. M. Woodley, *Phys. Chem. Chem. Phys.*, 2009
DOI: 10.1039/b902603g

Band gap engineering of ZnO *via* doping with manganese: effect of Mn clustering
Hilkka Saal, Thomas Bredow and Michael Binnewies, *Phys. Chem. Chem. Phys.*, 2009
DOI: 10.1039/b901596e

Transport pathways for mobile ions in disordered solids from the analysis of energy-scaled bond-valence mismatch landscapes
Stefan Adams and R. Prasada Rao, *Phys. Chem. Chem. Phys.*, 2009
DOI: 10.1039/b901753d

Ultrathin oxide films and heterojunctions: CaO layers on BaO and SrO
Chris E. Mohn, Neil L. Allan and John H. Harding, *Phys. Chem. Chem. Phys.*, 2009
DOI: 10.1039/b822588e

Formation entropies of intrinsic point defects in cubic In_2O_3 from first-principles density functional theory calculations
Péter Ágoston and Karsten Albe, *Phys. Chem. Chem. Phys.*, 2009
DOI: 10.1039/b900280d

Hydrogen adsorption on Pd-containing Au(111) bimetallic surfaces
Sudha Venkatachalam and Timo Jacob, *Phys. Chem. Chem. Phys.*, 2009
DOI: 10.1039/b900250b

Interdiffusion and surface-sandwich ordering in initial Ni-core–Pd-shell nanoparticle
Alexander V. Evteev, Elena V. Levchenko, Irina V. Belova and Graeme E. Murch, *Phys. Chem. Chem. Phys.*, 2009
DOI: 10.1039/b822112j

First-principles study on defect chemistry and migration of oxide ions in ceria doped with rare-earth cations
Masanobu Nakayama and Manfred Martin, *Phys. Chem. Chem. Phys.*, 2009
DOI: 10.1039/b900162j**An electrochemical study of lithium insertion into $Cr_{5-y}Ti_ySe_8$ (y = 1, 2, 3, 4, 4.5) beyond the intercalation limit**
Sylvio Indris, Joseph Wontcheu and Wolfgang Bensch, *Phys. Chem. Chem. Phys.*, 2009
DOI: 10.1039/b822397a

Mixed $LiCo_{0.6}M_{0.4}PO_4$ (M = Mn, Fe, Ni) phosphates: cycling mechanism and thermal stability
Natalia N. Bramnik, Dmytro M. Trots, Heiko J. Hofmann and Helmut Ehrenberg, *Phys. Chem. Chem. Phys.*, 2009
DOI: 10.1039/b901319a

Changes in the crystal and electronic structure of $LiCoO_2$ and $LiNiO_2$ upon Li intercalation and de-intercalation
Sonja Laubach, Stefan Laubach, Peter C. Schmidt, David Ensling, Stefan Schmid, Wolfram Jaegermann, Andreas Thißen, Kristian Nikolowski and Helmut Ehrenberg, *Phys. Chem. Chem. Phys.*, 2009
DOI: 10.1039/b901200a

Partial oxidation of methanol on well-ordered V_2O_5(001)/Au(111) thin films
J. M. Sturm, D. Göbke, H. Kuhlenbeck, J. Döbler, U. Reinhardt, M. V. Ganduglia-Pirovano, J. Sauer and H.-J. Freund, *Phys. Chem. Chem. Phys.*, 2009
DOI: 10.1039/b822384j

Investigation of the nucleation and growth dynamics of FePt nanoparticles prepared *via* a high-temperature synthesis route employing $PtCl_2$ as platinum precursor
Hauke Heller, Kirsten Ahrenstorf, Jose A. C. Broekaert and Horst Weller, *Phys. Chem. Chem. Phys.*, 2009
DOI: 10.1039/b822306h

Non-oxidic nanoscale composites: single-crystalline titanium carbide nanocubes in hierarchical porous carbon monoliths
Kirstin Sonnenburg, Bernd M. Smarsly and Torsten Brezesinski, *Phys. Chem. Chem. Phys.*, 2009
DOI: 10.1039/b822437d

Poly(p-phenylene sulfone)s with high ion exchange capacity: ionomers with unique microstructural and transport features
C. C. de Araujo, K. D. Kreuer, M. Schuster, G. Portale, H. Mendil-Jakani, G. Gebel and J. Maier, *Phys. Chem. Chem. Phys.*, 2009
DOI: 10.1039/b822069g

Pulsed electrodeposition of porous ZnO on Ag-coated polyamide filaments
Melanie Rudolph, Thomas Loewenstein, Elisa Arndt, Yvonne Zimmermann, Andreas Neudeck and Derck Schlettwein, *Phys. Chem. Chem. Phys.*, 2009
DOI: 10.1039/b822534f

Micro-ionics: next generation power sources

Harry L. Tuller,* Scott J. Litzelman and WooChul Jung

Received 29th January 2009, Accepted 9th March 2009
First published as an Advance Article on the web 25th March 2009
DOI: 10.1039/b901906e

The desire for ever smarter systems-on-a-chip and plug-free portable electronics with longer operating times between recharge has stimulated growing interest in micro-ionic systems. The use of thin film and photolithographic processing techniques, commonly at temperatures considerably below those utilized in conventional ceramics processing methods, leads to ionic or mixed ionic–electronic materials with nanosized dimensions. The implications for nanosized grains on the conductivity of thin film solid oxide electrolytes are examined. *Grain boundary engineering*, as a means of controlling and ultimately enhancing transport along and across grain boundaries, becomes essential given that such boundaries often dominate the transport properties of such nano-dimensioned materials. *Heterogeneous doping* by selective in-diffusion along grain boundaries was introduced as a potentially powerful means of achieving this. This is coupled with the modeling of space charge distributions at such boundaries, taking into account possible dopant segregation to the boundaries. The use of lithographic methods for generating geometrically well defined structures is used to illustrate how one can achieve a much improved understanding of electrode processes in SOFC structures. Indeed, the more idealized structures achievable by application of microelectronic processing provide a marvelous opportunity to uncover the science underlying the technology of micro- and ultimately macro-ionics.

Introduction

Nearly all areas of human activity have been impacted by the rapid progress that the microelectronics industry has achieved in extending the performance/cost ratio of modern integrated circuits. In particular, Si-based microelectronics are pervasive in communications, computation, automation, entertainment and nearly every endeavor in which the manipulation and flow of information, distribution of products or control of processes is involved. The near-ubiquitous use of silicon as the platform of the ever more sophisticated microelectronic devices is a reflection of its nearly unique combination of excellent electrical, mechanical, thermal and chemical properties combined with the ability to manufacture silicon wafers reproducibly at low cost.

This was not always the case. Microelectronics was preceded by vacuum tube electronics which was self-limiting in its abilities to address the needs of high speed computation and low cost portable electronics. Only the development of *solid state electronics*, by eliminating the need for electrons to pass through vacuum, enabled the extreme level of miniaturization and integration being achieved today. Stable operation was further achieved by isolating the *chips* as much as possible from environmental factors including humidity, temperature fluctuations, vibration and mechanical stresses. Packaging plays a strategic role in achieving desired performance ranging from hermetic packaging to thermal conduction modules that insure adequate heat dissipation.

Department of Materials Science and Engineering, Massachusetts Institute of Technology, Cambridge, MA 02139, USA. E-mail: tuller@mit.edu

Harry L. Tuller

Harry L. Tuller is Professor of Ceramics and Electronic Materials; Department of Materials Science and Engineering at Massachusetts Institute of Technology, and Editor-in-Chief of the Journal of Electroceramics. His research focuses on the science and technology of sensors, fuel cells; electroceramic thin films; microphotonics; thin film transistors and MEMS devices.

Scott J. Litzelman

Scott J. Litzelman received his BS from North Carolina State University, and the PhD degree in Material Science and Engineering at MIT under the direction of Prof. Tuller. His research interest includes nanoionic processes in solid state ionic devices.

In recent decades, the world has witnessed an extension of silicon technology from largely an electronic one to include mechanical (micro-actuators), optical (micro-mirrors), thermal (micro-heaters), chemical (micro-reactors) and biological (bio-chips) functions. This was achieved by the application of micromachining, extending the largely planar processing technology characteristic of microelectronics into the third dimension enabling the fabrication of membranes, micro-fluidic channels, micro-bridges and micro-cantilever beams to form what are now known as *microsystems or micro-electro-mechanical-systems* (MEMS).

Many of these newer applications, by their very nature, require the exposure of the silicon platform to the environment. Indeed, one is attempting to take advantage of the sensitive manner in which *microsystems* respond to variations in temperature, pressure or atmosphere. When we consider chemical functions, two areas, in particular, come to mind. The first category is sensors, of interest for environmental emissions monitoring and for process control in the petrochemical, food and pharmaceutical industries. Second, one visualizes the integration of miniaturized on-board power sources, important for portable and/or remote operation. In the latter case, fuel cells in particular require the input of often chemically aggressive fuels and oxidants and the subsequent removal of reaction products. In the following, we examine how opportunities in these areas are driving the *integration of solid state ionic and solid state electronic materials* in *microsystems* technology and, in the context of this special issue, how one can harness our understanding of the *science* of such materials to advance their *engineering*.

Solid state electrochemical devices

In the *solid state ionics* arena, there is much interest in reducing the operating temperatures of solid state oxide fuel cells (SOFCs) by shifting from bulk to thin film electrolytes (*e.g.* stabilized ZrO_2 or acceptor doped CeO_2). Indeed, the possibility thereby exists to embed miniaturized SOFC structures together with MEMS components, and other active electronics, into the same silicon wafer for portable power generation in devices such as laptop computers and mobile telephones.[1–5] In contrast to large-scale fuel cell stacks that

WooChul Jung

WooChul Jung received his BE from Seoul National University and is currently pursuing the PhD degree in Material Science and Engineering at MIT, under the direction of Prof. Tuller. His research interest includes the processing and characterization of thin film based solid state ionic devices (sensors and fuel cells).

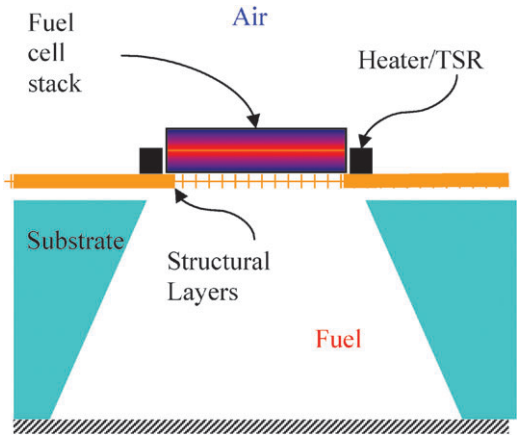

Fig. 1 Schematic of MEMS-based fuel cell showing characteristic anisotropically etched silicon wafer with thin film fuel cell stack with integrated heater and temperature sensitive resistor (TSR) supported on a perforated membrane.

output power of the order of megawatts, these micro-devices are intended to produce power of the order of milliwatts to several watts.

Battery technology has two shortcomings, namely, lower energy density (*e.g.* 130 W h kg^{-1} for lithium-ion rechargeable batteries) and long recharge times. Fuel cell devices, on the other hand, can tap the high energy densities of liquid hydrocarbon fuels (*e.g.* 6200 W h kg^{-1} for methanol) and are readily recharged.[6] Present solid state oxide fuel cell (SOFC) designs suffer from high operating temperatures (~800–1000 °C) necessary to raise the ionic conductivity of the electrolytes to suitable values. This requires costly ceramic interconnects and leads to enhanced chemical reaction between electrolyte and cathode, deterioration of electrode porosity and need for complex high temperature gas seals. MEMS-based designs, with thin film self-supporting electrolytes and highly catalytically active electrodes, see Fig. 1, promise significantly reduced processing and operating temperatures, leading to extended life and reduced cost.

To understand where the challenges lie in enabling a reduced operating temperature conventional or micro SOFC, we turn to the schematic of an operating fuel cell stack in Fig. 2. This diagram illustrates the concentration gradient driven transfer of gaseous molecular oxygen from the cathode to the anode *via* the electrolyte as an ion and its subsequent reaction at the anode with hydrogen to form water. The reaction proceeds by the simultaneous transfer of electrons from the anode to the cathode *via* the external load. The corresponding electrochemical reactions occurring at the cathode and anode are given, respectively, by:

$$O_2 + 4e' + V_O^{\bullet\bullet} \Leftrightarrow 2O_O \quad (1)$$

$$2O_O + 2H_2 \Rightarrow 2H_2O + 4e' \quad (2)$$

where $V_O^{\bullet\bullet}$ and O_O represent doubly charged oxygen vacancies and oxygen ions, respectively, on oxygen ion lattice sites in the crystal structure. All other terms have their normal meanings.

The key operating losses result from the resistance of the polycrystalline electrolyte which includes both bulk ionic transport within the grains (dotted arrow) and contributions

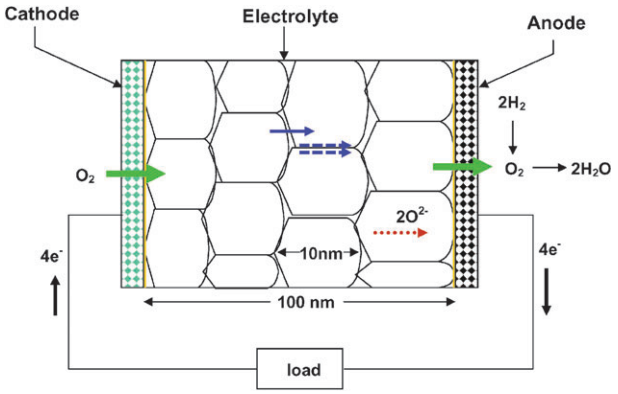

Fig. 2 Schematic of a solid oxide fuel cell illustrating the transfer of gaseous molecular oxygen from the cathode to the anode *via* the electrolyte as an ion and its subsequent reaction at the anode with hydrogen to form water. The reaction proceeds by the simultaneous transfer of electrons from the anode to the cathode *via* the external load.

due to ionic transport across (solid thin arrow) or along grain boundaries (dashed arrows) and the electrochemical reactions at the electrodes (solid thick arrows). Fortunately, it is possible to deconvolute these various losses by the application of electrochemical impedance spectroscopy (EIS) as illustrated in Fig. 3. For the idealized case, in which each of the above processes (*i.e.* bulk, grain boundary and electrode) can be modeled by a simple parallel resistor–capacitor network, a semicircle for each is defined in the complex impedance plane representing the impedance vector sweeping out the spectrum as the excitation frequency is varied typically from the mHz to the MHz range. The diameter of each semicircle is a measure of the resistance, R, while the frequency at the peak of the semicircle is given by $\omega_{peak} = 1/RC$. The spectrum illustrated in Fig. 3 assumes that the RC time constants of the different processes differ considerably and that the capacitances decrease from the very large values associated with electrode processes, to intermediate capacitances exhibited by space charge layers at grain boundaries, to the low capacitances corresponding to bulk capacitances. Examples of the use of EIS in isolating and investigating individual processes are presented later in this paper.

Much of the remainder of this article will be concerned with how one should approach achieving a reduction in these losses

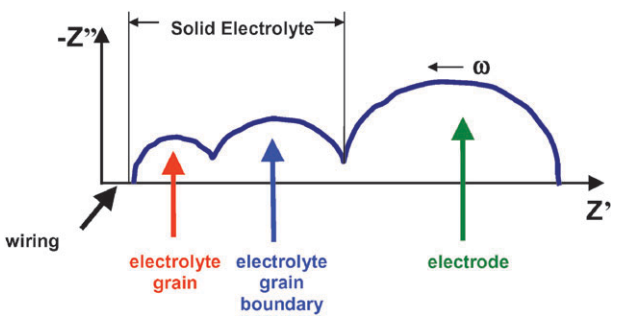

Fig. 3 Electrochemical impedance spectrum demonstrating the ability to deconvolute grain, grain boundary and electrode contributions. See text for details.

by investigating the underlying science related to defect formation, and corresponding mass and charge transport in nanostructured mixed ionic–electronic conductors (MIEC). Ideally, these and other insights will be harnessed to advance the engineering of reduced temperature and micro fuel cells.

Nanodimensional films

The most obvious source of loss in an SOFC is the ohmic electrolyte resistance given by $R = (1/\sigma)(l/A)$, in which σ is the electrical conductivity, and l/A is the length over area ratio of the resistor. There have been many attempts over the decades to identify materials with higher ionic conductivities than that of yttria stabilized zirconia (YSZ), the standard solid electrolyte used in SOFCs. Notable examples include the fluorite structured gadolinium doped ceria ($Gd_xCe_{1-x}O_{2-\delta}$; GDC) and the perovskite structured lanthanum strontium gallium magnesium oxide ($(La_{1-y}Sr_y)(Ga_{1-x}Mg_x)O_{3-\delta}$; LSGM).[7] While these compounds are more highly conductive than YSZ, particularly at reduced temperatures, they tend to be less chemically and/or mechanically stable. Thus, in recent years, there has been an increasing focus on a strategy for reducing the electrolyte resistance by substantially reducing the electrolyte thickness, l, by switching from bulk ceramic or thick-film techniques to thin film processing technology. Indeed, solid electrolyte membranes of ~150 nm thickness would provide adequate electrolyte conductance down to temperatures of ~200 and 400 °C with CGO and YSZ, respectively.[8–11] Because such thin films are commonly characterized by features with nano-dimensions, other factors come into play regarding performance, leading to either improved or degraded properties. As a consequence, nanosize effects are considered, in some detail, in the following.

Oxide films deposited by physical or chemical routes are typically submicron in thickness. Given the low temperature processing routes typically utilized, this often results in polycrystalline morphologies in which the grains are in the tens of nanometres in dimension. The resulting morphologies lead to conditions in which the effective grain boundary widths (including space charge effects discussed below) approach that of the cross sectional dimensions of the grains. The question that then naturally arises is: does transport along the grain boundaries become comparable to or exceed that within the grains and, if it does, can this be used to improve the ionic conduction properties of the electrolyte film?

Beginning in 1996, the author and co-workers reported that the electrical conductivity of bulk nanocrystalline CeO_2 increased substantially over that of coarsened microcrystalline CeO_2[12,13] as a result, in that case, of increased electronic conductivity. Subsequently, Tschöpe[14] and Kim and Maier[15] attributed the increase in electronic conductivity and decrease in ionic conductivity to space charge effects resulting from segregation of positive charges to the grain boundary cores. Similar effects were reported more recently by the author in vapor phase deposited ceria thin films with nanosized grains.[16] This suggests that film microstructure, in addition to composition, can be used to control the mix of ionic and electronic conductivities. In the following, we examine the theory in some detail, examine implications for technology and review

the limited attempts, to date, to apply these concepts towards the development of improved devices.

Properties of space charge regions

Ionic solids, while neutrally-charged overall, commonly contain local areas of electrostatic charge known as space charge regions. Crystalline symmetry is broken at interfaces such as grain boundaries and surfaces, and the subsequent redistribution of anions and cations leads to local charge. The space charge potential, $\Delta\phi = \phi(0) - \phi(\infty)$, where $\phi(0)$ is the potential at the interface and $\phi(\infty)$ is the reference value in the bulk, determines the charge carrier profiles in the space charge layer. This section quantitatively describes the spatial variation of ionic and electronic defects within the space charge layer.

The equilibrium condition for species j between two locations, $x1$ and $x2$, is given by the constancy of the electrochemical potential:

$$\tilde{\mu}_j(x1) = \tilde{\mu}_j(x2) \tag{3}$$

consisting of the chemical potential, μ, and electrostatic potential, ϕ:

$$\tilde{\mu}_j(x) = \mu_j(x) + z_j e\phi(x) \tag{4}$$

where $z_j e$ is the net charge. For dilute defect concentrations, the chemical potential term in eqn (5) can be expanded to include the standard chemical potential, μ_j^0, and the concentration† c_j of species j.

$$\mu_j = \mu_j^0 + kT \ln c_j \tag{5}$$

Substituting into eqn (4), the following electrochemical equilibrium is obtained:

$$\mu_j^0 + kT \ln c_j(x1) + z_j e\phi(x1) = \mu_j^0 + kT \ln c_j(x2) + z_j e\phi(x2) \tag{6}$$

or

$$\frac{c_j(x2)}{c_j(x1)} = \exp\left[-z_j e\left(\frac{\phi(x2) - \phi(x1)}{kT}\right)\right] \tag{7}$$

or expressing the change in space charge concentration relative to the bulk concentration as a function of the local electrical potential:

$$\left(\frac{c_j(x)}{c_{j\infty}}\right)^{1/z_j} = \exp\left(-\frac{e}{k_B T}\Delta\phi(x)\right) \tag{8}$$

These equations demonstrate that an *electrical potential difference is compensated by nonuniform chemical profiles* in order to preserve electrochemical equilibrium.

In order to find the concentration profiles, one must solve for the spatial variation of the electrical potential. Poisson's equation:

$$\nabla^2\phi = -\frac{\rho}{\varepsilon_o\varepsilon_r} = -\frac{z_j e c_j}{\varepsilon_o\varepsilon_r} \tag{9}$$

† Normalized concentration.

can be combined with eqn (8) to form the Poisson–Boltzmann differential equation, here treated for the case of electrostatic potential variation in one dimension:‡

$$\frac{d^2\phi}{dx^2} = -\frac{e z_j c_{j\infty}}{\varepsilon_o\varepsilon_r}\exp\left(\frac{-z_j e}{kT}\Delta\phi(x)\right) \tag{10}$$

Applying appropriate boundary conditions and a reference point for the potential, commonly set to 0 in the bulk, yields the spatial variation of the electrostatic potential under Gouy–Chapman conditions, which specifies the redistribution of all charged defects:[17]

$$\phi(x) = \frac{2kT}{z_j e}\ln\left(\frac{1 + \Theta\exp(-x/\lambda)}{1 - \Theta\exp(-x/\lambda)}\right) \tag{11}$$

where λ is the Debye length:

$$\lambda = \sqrt{\frac{\varepsilon_o\varepsilon_r kT}{2z_j^2 e^2 c_{j\infty}}} \tag{12}$$

and Θ is the profile parameter:

$$\Theta = \tanh\left(\frac{z_j e\Delta\phi}{4kT}\right) \tag{13}$$

The charge density σ and the space charge potential ϕ(o) are related by:

$$\sigma = \sqrt{8kTc_{j\infty}\varepsilon_o\varepsilon_r}\sinh\left(\frac{ze\phi(0)}{2kT}\right) \tag{14}$$

Finally, by combination of eqn (8) and (11), the spatial profiles of defects in the space charge region are found:

$$\frac{c_j(x)}{c_{j\infty}} = \left(\frac{1 + \Theta\exp(-x/\lambda)}{1 - \Theta\exp(-x/\lambda)}\right)^{2z_j} \tag{15}$$

The Gouy–Chapman analysis above is valid only when all defect species can redistribute in the space charge region. At reduced temperatures, it is often the case that the defect controlling the Debye length is insufficiently mobile to redistribute in response to the excess grain boundary charge. In this case, the depleted defects are often neglected, and the charge density in Poisson's equation is determined only by the dopant content. This is known as the Mott–Schottky approximation,[18,19] and the immobile carrier *e.g.* in ceria is typically the ionized background acceptor. Poisson's equation is simplified and becomes

$$\frac{\partial^2\phi}{dx^2} = -\frac{z_j e c_{j\infty}}{\varepsilon_o\varepsilon_r} \tag{16}$$

and with boundary conditions $\phi'(\lambda^*) = 0$ and $\phi'(\lambda^*) = \phi_\infty = 0$ can be integrated to yield (relative to the bulk reference potential, commonly set to zero):

$$\Delta\phi(x) = -\frac{z_j e c_{j\infty}}{\varepsilon_o\varepsilon_r}(x - \lambda^*)^2 \tag{17}$$

‡ Here concentration in terms of cm^{-3}.

where λ^* is the depletion (space charge) width:[19]

$$\lambda^* = \sqrt{\frac{2\varepsilon_o\varepsilon_r\Delta\phi(0)}{z_j e c_{j\infty}}} = \lambda\sqrt{\frac{4z_j e}{kT}\Delta\phi(0)} \qquad (18)$$

Two distinct differences can be seen in the relation for the space charge width in the Mott–Schottky boundary conditions compared to Gouy–Chapman. When the majority defect cannot redistribute, the space charge width is dependent on the space charge potential, and the depletion width is greater in spatial extent due to a reduced charge screening ability. The expression for the potential difference as a function of x can be substituted into the original equation for carrier enhancement/depletion to give the concentration dependence:

$$\frac{c_i(x)}{c_{i\infty}} = \exp\left[-\frac{z_i}{z_j}\left(\frac{x-\lambda^*}{2\lambda}\right)^2\right] \qquad (19)$$

where defect i is enhanced or depleted, and defect j is the majority defect that determines the space charge width. For oxygen vacancies depleted in the space charge region, $z_i = 2$ and $z_j = 1$ while for electrons which are accumulated, $z_i = -1$ and $z_j = 1$. Taking the ratio of the two terms:

$$\frac{c_n(x)}{c_{n\infty}} = \left(\frac{c_V(x)}{c_{V\infty}}\right)^{-1/2} \qquad (20)$$

it is clear that a ten-fold decrease in the electron concentration $c_n(x)$ would result in a hundred-fold increase in the oxygen vacancy concentration $c_V(x)$. This feature will be referred to in subsequent discussion of experimental results.

To facilitate visualization of the difference in defect profiles for these two models, schematic profiles are plotted in Fig. 4 for the predominant defects in ceria for a space charge potential of 0.4 V and an acceptor concentration of 300 ppm at 500 °C. Under these conditions, *depletion of oxygen vacancies* and *enhancement of electrons* are predicted in both models in response to a positive potential in the grain boundary core. It is evident, however, that the natures of the profiles differ considerably. In the Gouy–Chapman case, there is a very large change in carrier concentration within only the first few nanometres from the grain boundary core. Thus, most of the enhancement/depletion effects occur approximately within one Debye length. Under Mott–Schottky conditions, the change in carrier concentration is less severe. On the other hand, the extent of non-uniformity is much larger than the Debye length, due to reduced charge screening resulting from the immobile acceptor.

While eqn (15) and (19) predict that the concentration of mobile, positively charged, oxygen ion defects ($V_O^{\bullet\bullet}$) could be markedly enhanced if the trapped charges at the boundary were negative, all experimental evidence to date suggests that the boundaries in ceria and zirconia based solid oxide electrolytes are inherently positive,[14,15,20] thereby leading instead to a decrease of the ionic conductivity and an increase in electronic conductivity with decreasing grain size for ceria as illustrated in Fig. 5.[21] Indeed, while enhanced ionic conduction resulting from space charge effects has been reported for Li and F ion conducting electrolytes,[22,23] no clear evidence for space charge induced enhanced oxygen ion conduction has been reported to date.

Heterogeneous doping of solid electrolytes

The electrical conductivity of an ionic solid is typically controlled by homogeneous doping, in which donor and/or acceptor species substitute on lattice sites or enter the structure interstitially. Ideally, such doping occurs uniformly throughout the material, and the charged impurities are compensated by the formation of defects of opposite charge, either electronic or ionic, in order to preserve charge neutrality. There is, however, another method with which the electrical conductivity can, in principle, be controlled: *heterogeneous* doping. This concept was first demonstrated in dramatic fashion by Liang in 1973.[22] In that study, the *insulating*

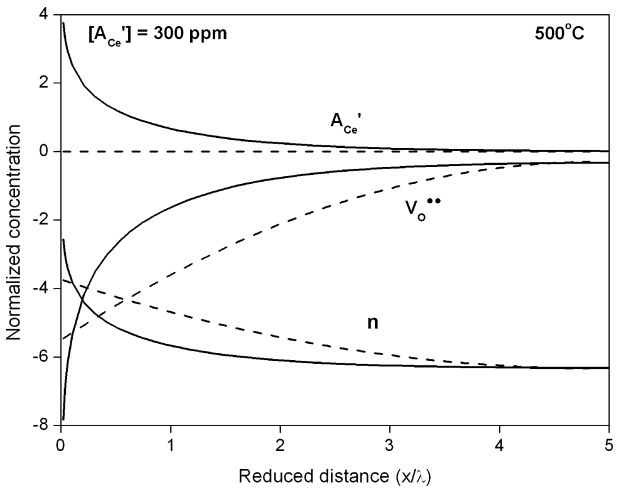

Fig. 4 Space charge profiles of acceptor dopants, oxygen vacancies, and electrons near a grain boundary interface with a space charge potential of +0.4 V, according to the Gouy–Chapman (solid lines) and Mott–Schottky (dotted lines) models. Concentrations normalized to dopant density.

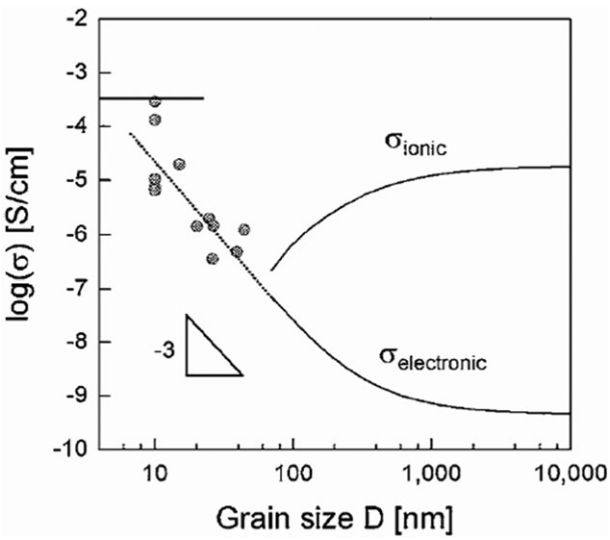

Fig. 5 The dependence of the ionic and electronic conductivities shows a strong dependence on grain size for grains below about 600 nm in diameter.[21]

compound Al_2O_3 was added as a second phase to the ionic conductor LiI, and the ionic conductivity was subsequently *increased* by up to 50 times relative to pure LiI.

While the improvement of ionic conductivity *via* an insulating phase may appear counter-intuitive, the concept was first discussed with respect to the space charge model by Wagner.[24] A thorough review and analysis of this effect was later presented by Maier.[25] Analogous to the discussion above, defects can be enhanced or depleted in a space charge layer induced at the heterojunction between the two phases, and the spatially-varying conductivity will depend on the relative mobility of the charge-carrying defects. In the LiI–Al_2O_3 system, the space charge layer is enhanced in the high-mobility I^{-1} species, resulting in enhanced ionic conductivity relative to the single phase. Other more recent examples of reports of appreciable improvements in ionic conductivity at hetero-interfaces include F ion conduction in BaF_2/CaF_2 multi-layers[23] and O ion conduction in $YSZ/SrTiO_3$ multilayers.[26] The logical question now emerges: are there other means by which heterogeneous doping may be employed to alter materials properties in a desirable manner but without creation of second phases? In the following, we summarize our recent attempts to achieve enhanced ionic conduction in nanocrystalline ceria films by selective doping of grain boundaries, *via* in-diffusion from surface diffusion sources.

The most common types of diffusion are bulk, grain boundary, surface, and along dislocations. It is well-known that diffusion in metals and ceramics along grain boundaries is typically much faster than in the bulk,§ often by 3–6 orders of magnitude.[27] Harrison described three distinct diffusion regimes that occur in a polycrystalline material.[28] These include (A) uniform diffusion throughout the material described by an effective diffusion coefficient that is a linear combination of the bulk and grain boundary processes; (B) unequal penetration with more rapid diffusion along grain boundaries, with slow but appreciable penetration into the bulk, particularly near the surface; and (C) negligible mass transport in the bulk with diffusion limited to the grain boundary regions. The latter regime is rarely reported in the literature, as it only occurs at low temperatures, and the small amount of diffusing species is often difficult to detect analytically.

Harrison C-regime diffusion suggests itself as an ideal means for modifying the chemical constituents at the grain boundary without modifying the chemistry of the grains. In ref. 16, the authors proposed heterogeneous doping of Ni and Gd along grain boundaries as a means to alter the space charge properties of nanocrystalline ceria. By selective diffusion of cationic species likely to change the net charge stored at the grain boundaries, *e.g.* negative charge created by $Ni_{Ce}^{2\prime}$, it should be possible to modify both the magnitude and polarity of the space charge potential as illustrated in Fig. 6. The requirements include: (a) grain boundary diffusivity $D_{GB} \gg D_b$, the bulk (or grain) diffusivity, and (b) the diffusion length be short enough so that the boundaries can be

§ This may not be the case in fast ion conductors for the more mobile species, but will still be the case for the less mobile species, *i.e.* for cations in fluorite structured materials such as ceria.

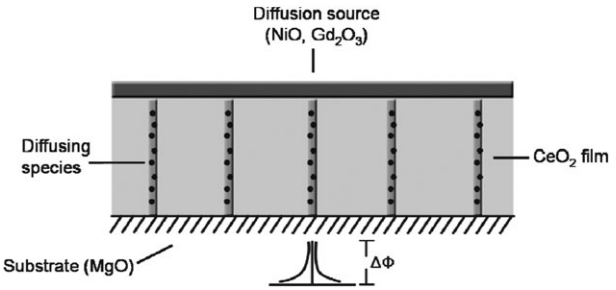

Fig. 6 Schematic of a ceria columnar film grown on an MgO substrate with Ni^{2+} or Gd^{3+} ions selectively diffused down the grain boundaries. The charged species are expected to modify the net charge of the boundaries and, as a consequence, the boundary potential, $\Delta\phi$.

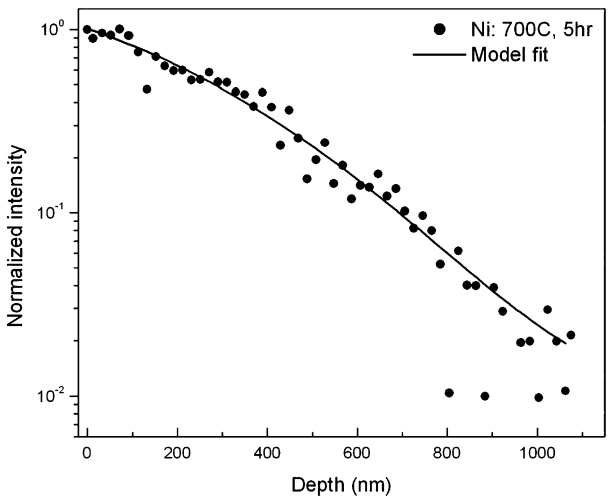

Fig. 7 In-diffusion profile of Ni into a ceria film of about 1 micron thickness following a 700 °C anneal for 5 h. A value of $D_{GB}(Ni) = 4.2 \times 10^{-14}$ cm^2 s^{-1} is derived from the fit to the penetration profile.[16]

uniformly doped. As demonstrated in Fig. 7 for Ni in-diffusion into pulsed laser deposited ceria thin films, Ni penetrates about 1 micron along the grain boundaries following only a five hour anneal at 700 °C with uniform distribution of the Ni achieved at 800 °C after a 10 h anneal.[16]

To test whether heterogeneous doping of ceria by Ni can indeed serve to reduce electronic conduction and enhance ionic conduction, the electrical conductivity of the films was measured prior to and following Ni in-diffusion. As shown in Fig. 8, the electrical conductivity of Ni and Gd in-diffused ceria films dropped about an order of magnitude below that of the as-deposited films. Both in-diffused and as-deposited films exhibited a $pO_2^{-1/4}$ dependence of the conductivity (not shown) suggesting that the conductivity in both cases was largely electronic in nature. The approximately ten-fold decrease in electronic conductivity, consistent with a decrease in the magnitude of the positive boundary potential, suggests that while the in-diffused Ni was unable to reverse the polarity of the grain boundary, it was able to decrease its magnitude. Because the oxygen ion vacancies are doubly positively charged, a ten-fold decrease in electronic carriers due to a change in potential should be accompanied by a hundred-fold increase in ionic carrier concentration, c_V, as discussed above

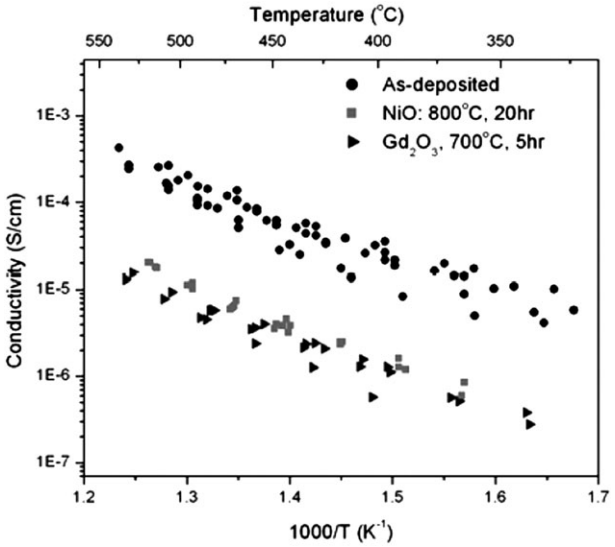

Fig. 8 The total electrical conductivity measured as a function of temperature for as-deposited and for Ni and Gd in-diffused ceria thin films.

(see eqn (20)). Nevertheless, the ionic conductivity could easily remain the minority conductivity type if the potential barrier was large enough initially to depress ionic carriers by many orders of magnitude (see Fig. 5). Therefore, to be able to test the expectation of a much enhanced ionic conductivity resulting from heterogeneous doping, the much larger electronic conductivity would have to be blocked by an ionic conductor in series with the ceria test film.[29]

Electron blocking experiments were initiated, taking particular care to insure that the results were not dominated by redox reactions at the electrode surfaces or triple phase boundaries.[30] The results shown in Fig. 9 confirm that indeed the as-deposited film is dominated by a pO_2 dependent electronic conductivity with a nearly pO_2 independent minority ionic conductivity. Surprisingly, however, while the ionic conductivity was an order of magnitude lower than the electronic conductivity at $pO_2 = 10^{-3}$ atm, they were nearly

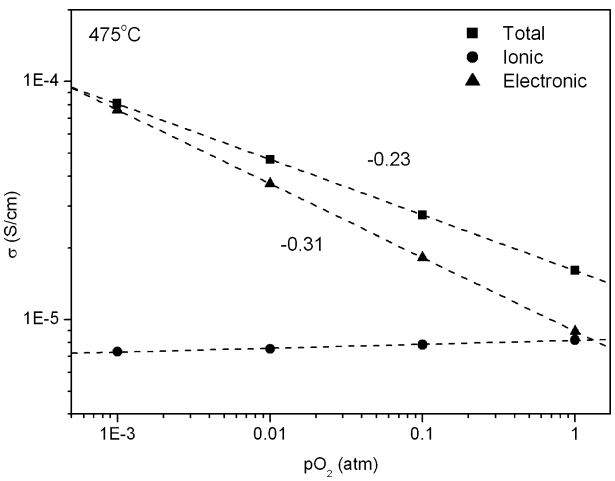

Fig. 9 Electrical conductivity *vs.* pO_2 on an as-deposited thin film *via* blocking electrodes, measured at 475 °C. Shown are the total (■), ionic (●), and electronic (▲) conductivities.

equal to each other at 1 atm. It then becomes difficult to understand why the ionic conductivity was not observed to dominate the Ni in-diffused specimen, if indeed the ionic conductivity increased by a hundred-fold.

Subsequent blocking measurements performed on both in-diffused specimens as well as untreated films, which had been subsequently exposed to the same high temperature anneals as the in-diffused specimens, revealed that, in all cases, and opposite to expectations, the ionic conductivity rather than being enhanced was depressed along with the electronic conductivity by the treatments, as illustrated in Fig. 10.

Following Maier's approach for calculating the space charge contributions to the observed conductivity,[31] the perpendicular and parallel conductivities associated with electrons and oxygen vacancies for both the Gouy–Chapman and Mott–Schottky models were calculated.[32] The closest analytical description of the experimental data occurs for the Mott–Schottky model with a grain size of 35 nm and $\Delta\Phi = 0.44$ V in the as-deposited state, and the Gouy–Chapman model with a grain size of 75 nm and $\Delta\Phi = 0.35$ V after annealing in the presence of a diffusion source. After annealing, it is evident that both the ionic and electronic partial conductivities decrease, which is inconsistent with a shift in the space charge potential alone. If the acceptor impurities are assumed to be sufficiently mobile to redistribute at temperatures of 700 °C and above, the Gouy–Chapman model correctly predicts a decrease of both partial conductivities, though not in the correct proportion. The agreement with the experimental data is markedly improved if the space charge potential is decreased from 0.44 to 0.35 V which would require only a decrease in charge at the boundary from $Q_{core} = 7.31 \times 10^{-20}$ C nm^{-2} to $Q_{core,after} = 6.52 \times 10^{-20}$ C nm^{-2}, a difference of approximately 8×10^{-21} C nm^{-2}. This difference would require a change in dopants at the boundary of 5×10^{12} cm^{-2} or, equivalently, a change in cation composition at the boundary of only 0.6%. Several experimental observations remain unexplained. The reason for

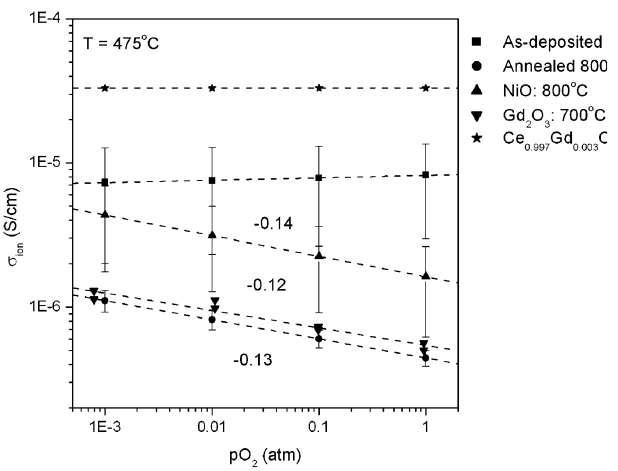

Fig. 10 Ionic conductivity *vs.* pO_2 for various specimens. Shown are data from as-deposited samples (■), as well as samples annealed with no diffusion source (●), a NiO (▲) and Gd_2O_3 source (▼). Shown for reference is the ionic conductivity of CeO_2 homogeneously doped with 0.3 cat% Gd (star).

the shift in the pO_2 dependence of σ_{ion} from 0 to −0.13 is unclear. This problem is compounded by the overall lack of understanding of the pO_2 dependence of the space charge potential. Numerical modeling is needed to predict field and carrier distributions for conditions neither satisfied by the Gouy–Chapman nor the Mott–Schottky model due to kinetic or other considerations.

Electrode processes

Even if the ohmic and grain boundary resistances of the electrolyte can be reduced to desired levels, this still leaves the large polarization losses exhibited by the cathode and anode at reduced temperatures. Given that electrode losses are, by and large, limited to interfacial processes, reduction in their thickness, in contrast to the electrolyte, is not expected to improve performance. On the other hand, simultaneously high levels of ionic and electronic conductivities in the electrode materials appear to lead to considerably reduced losses at reduced temperatures, as exemplified by the MIEC perovskite $La_{1-x}Sr_xCoO_3$ (LSC) as compared to $La_{1-x}Sr_xMnO_3$ (LSM), whose ionic conductivity is orders of magnitude lower at temperatures of 500–700 °C.[33] Both to test the generality of this hypothesis and to investigate it more systematically, we selected an alternate perovskite system, $SrTi_{1-x}Fe_xO_3$ (STF), in which both the ionic and electronic conductivities could be systematically varied, and by orders of magnitude, by control of the Fe fraction, x.

Before going on, it is useful to examine the various processes which potentially impact cathode performance. A schematic of the cathode and electrolyte interface, Fig. 11, shows the various kinetic steps needed for the incoming O_2 molecule to diffuse, adsorb, dissociate, and ionize before it can be incorporated into the electrolyte as the O^{2-} ion. Cathodes which do not support significant ionic conduction such as LSM are limited in their ability to reduce oxygen to the ion and insert it into the electrolyte to the triple phase boundary between gas, cathode and electrolyte (dark line between cathode and electrolyte in Fig. 11) while MIEC cathodes allow all the key reactions to occur over the full surface of the cathode. Surprisingly, even after many decades of study, a consensus still does not exist regarding which of the possible kinetic steps is limiting cathode performance for even the most popular cathode materials.[34–37] This, in part, is related to the

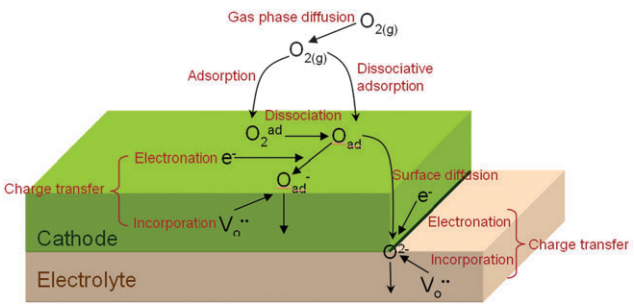

Fig. 11 Schematic of the gas, cathode and electrolyte interfaces showing the various kinetic steps needed for the incoming O_2 molecule to diffuse, adsorb, dissociate, and ionize before it can be incorporated into the electrolyte as the O^{2-} ion.

complex and difficult-to-replicate morphology of the cathode–electrolyte interface, characteristic of most systems prepared by conventional ceramic and/or thick film processing technologies.

To overcome the complexities in examining and understanding typical electrode–electrolyte systems, two key factors need attention. First, it is desirable to have a cathode material system which can be systematically modified with respect to the relative magnitudes and ratios of achievable ionic and electronic conductivities exhibited by the system. This allows one to test the role of the mixed conductivity in limiting mass and charge transport within the cathode. Controlling the energy band structure allows one to investigate the significance of energy level alignments in controlling charge transfer processes. The $SrTi_{1-x}Fe_xO_{3-\delta}$ system (STF) forms a continuous solid solution over the entire composition range $0 < x < 1$,[38] with substitution of Fe for Ti resulting in a systematic decrease in band gap due to the introduction of the Fe derived impurity band (see Fig. 12). The introduction of the lower valent Fe further results in an increase in electron, hole and oxygen vacancy density (see Fig. 13), providing, in turn, mixed conductivity with high levels of electronic and ionic conductivities at elevated levels of x.[39] The defect structure, transport properties and band structure of the STF perovskite, previously examined in detail, thereby allow for the prediction of these properties for controlled temperatures, pO_2s and Fe levels.[39,40]

Secondly, the geometry and morphology of the electrodes should be as simple as possible to enable one to easily distinguish between reactions which are limited at the triple phase boundaries and the full surface area of the electrodes. Geometrically simple and reproducible dense, thin film model electrode structures, *e.g.* fabricated by vacuum based physical vapor deposition (PVD) methods, readily fulfill these requirements.[41–44] In this manner, precise control of both triple phase boundary length (TPBL) and area allows for a quantitative analysis of the electrochemical properties by normalization of the experimental data with respect to geometry, *i.e.* triple phase boundary length (TPBL), surface area, film thickness and surface roughness. Furthermore, features such as crystal orientation, grain size and shape, and compositional variations can be varied by control of deposition conditions, *i.e.* deposition temperature, pressure, power, gas composition, substrate composition, *etc.*

To test their cathodic behavior, polycrystalline STF thin films, with highly (110) orientated texture, grain sizes of between 100 and 200 nm, surface roughness of ~2 nm and film thicknesses ranging between 70 and 440 nm, were deposited by pulsed laser deposition (PLD) onto (100) oriented single crystal yttria doped zirconia (YSZ) substrates. Fig. 14 shows the different diameter circular films of STF deposited by PLD onto a single crystal wafer of YSZ with overlays emphasizing the different areas, perimeters and thicknesses of the electrodes. A symmetrical structure with identically sized STF electrodes on both sides of the YSZ electrolyte was used for impedance spectroscopy (IS) measurements.

Fig. 15 shows typical impedance results obtained for the symmetrical structure in which the STF electrodes with composition $x = 0.35$, designated as STF35, are characterized

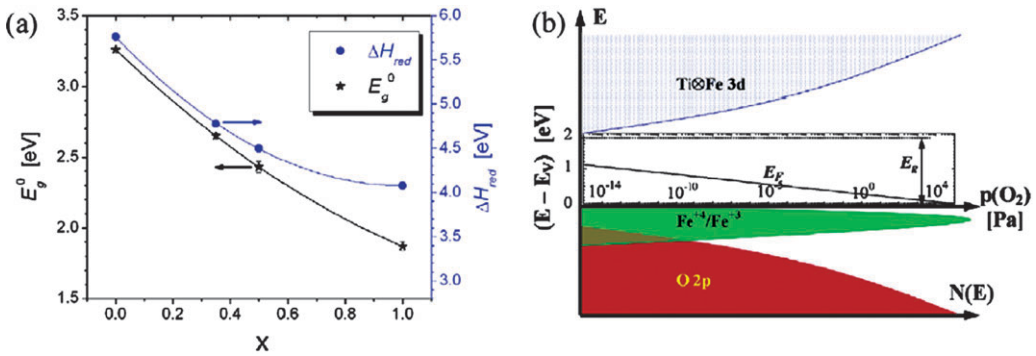

Fig. 12 (a) A plot of the band gap energy and reduction enthalpy in the STF system as a function of Fe fraction, x. (b) Energy band diagram (energy *vs.* density of states N(E)) of the STF system showing the O2p derived valence band, the largely Ti3d derived conduction band and the Fe3d derived impurity band.

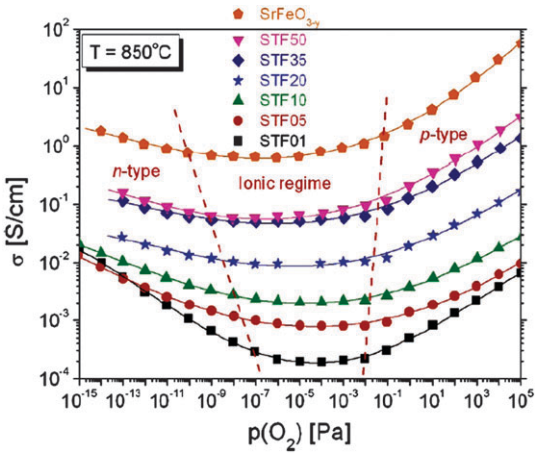

Fig. 13 Electrical conductivity isotherm, at 850 °C, as a function of oxygen partial pressure for different STF compositions with Fe concentrations between 1 mol% (STF01) and 100 mol% ($SrFeO_{3-y}$).

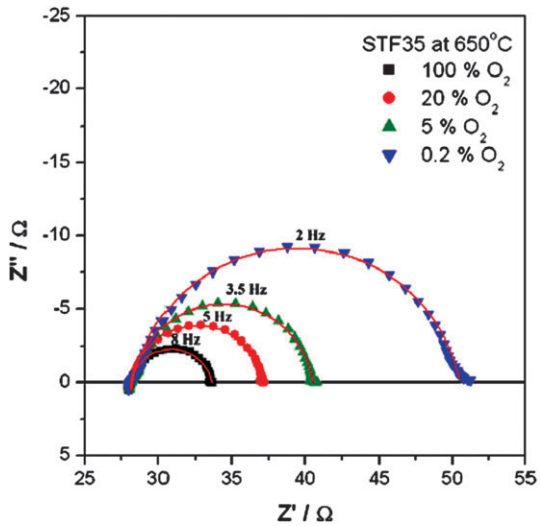

Fig. 15 Impedance spectroscopy plots of STF35 at T = 650 °C at various oxygen partial pressures.

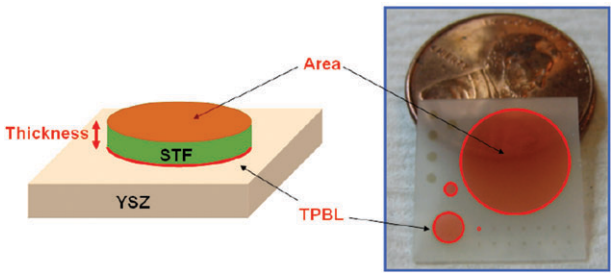

Fig. 14 The figure on the right shows different diameter circular films of STF deposited by PLD onto a single crystal wafer of YSZ with overlays emphasizing the different areas and perimeters of the electrodes. A US one cent coin in the background provides scale. The schematic on the left illustrates the location of the triple phase boundary and that the film thickness, along with area and triple phase boundary length, is a key geometric parameter.

by an offset resistance (R_{off}) followed by a nearly ideal semicircle at low frequencies (LF). R_{off} is attributed to the ohmic resistance of the YSZ electrolyte based on its activation energy (~0.95 eV), its pO_2 independence and the calculated value of the equivalent conductivity.

The use of dense thin film electrodes with simple geometry enables one to obtain a quantitative relationship between electrode impedance and geometry. A power law dependence of approximately −2 (rather than −1) for the dependence of log R_{LF} on log electrode diameter (1–10 mm) (see Fig. 16) confirms that the electrode resistances are inversely proportional to electrode surface area, rather than to the triple phase boundary length (TPBL). One can thus conclude that the oxygen reduction reaction occurs largely over the electrode surface area, rather than being limited to the TPB, as also reported for thin film LSC and LSCF MIEC electrodes.[41,45,46] Furthermore, the near independence of R_{LF} on electrode thickness (see Fig. 17) eliminates mass transport through the electrode as the limiting step. Finally, the insensitivity of R_{LF} to the insertion of a ceria –gadolinia (CGO) interlayer between the electrolyte and the STF electrode, not shown, confirms that interfacial transfer between the electrolyte and the electrode is not limiting (see Fig. 18). One therefore concludes that there is a common limiting process for nearly the full STF solid solution system (x = 0.05 to 1.0 studied to date) which must be attributed to the surface oxygen exchange reaction

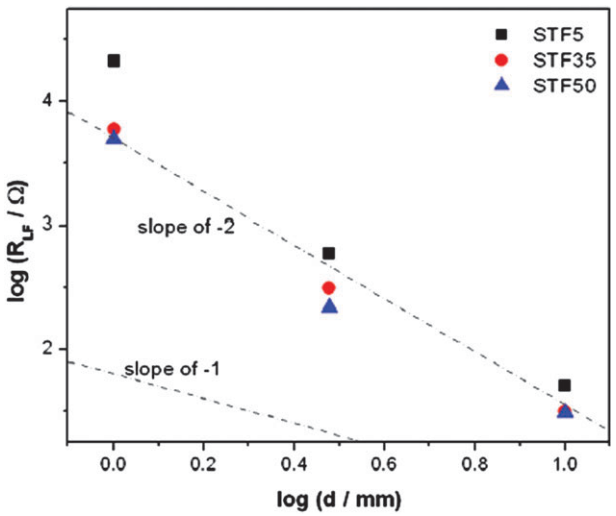

Fig. 16 Double-logarithmic plots of R_{LF} *vs.* diameter measured for STF5, STF35 and STF50 electrodes at 590 °C in air.

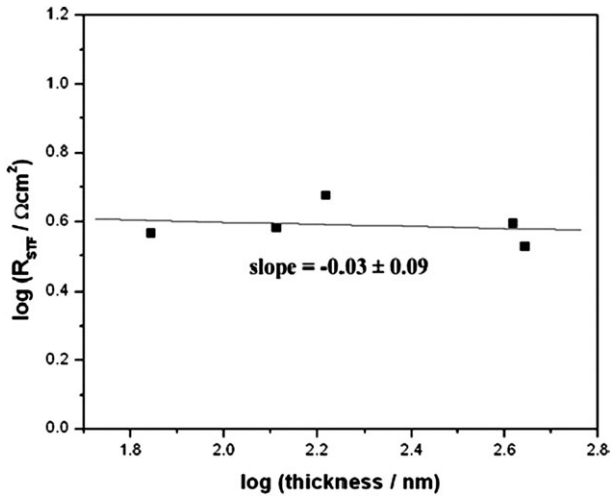

Fig. 17 Double-logarithmic plots of the ASR (R_{STF}) of a STF50 electrode *vs.* its thickness measured at 650 °C in air.

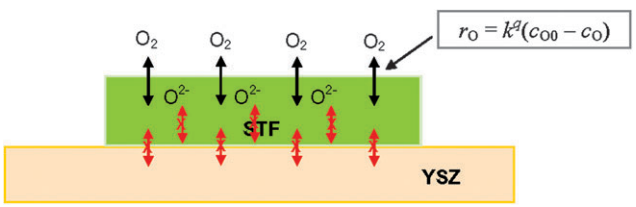

Fig. 18 Surface exchange kinetics were found to be the rate limiting step controlling the electrode impedance. The thickness independence of R eliminates diffusion limitations through the electrode while insensitivity of R to the insertion of a CGO interlayer between STF and YSZ eliminates interfacial transport across that interface as the rate limiting step. The rate equation relates the oxygen arrival rate r_O to k^q, the exchange rate, c_O, the oxygen concentration at the interface, and c_{O0}, the oxygen concentration in the gas phase.

occurring at the surface of the STF electrodes. For surface exchange controlled kinetics, the oxygen surface exchange coefficient k^q can be extracted from the electrode resistance by:[47]

$$k^q = \frac{kT}{4e^2 R_s c_o} \tag{21}$$

in which R_s is the area specific resistance and c_o is the total concentration of lattice oxygen (STF: $\sim 5 \times 10^{22}$ cm^{-3}).[39]

The area specific resistance (ASR) of the STF electrodes, plotted as a function of reciprocal temperature in Fig. 19, exhibits a gradual reduction with increasing Fe fraction largely saturating for Fe levels above STF35. Because the ASR decreases by only approximately a factor of 10 in going from STF5 to STF80 while the ionic and electronic conductivities increase by about a factor of 1000,[39] this suggests that the surface exchange kinetics are, at best, weakly influenced by the bulk electrical properties of STF. This insensitivity is clearly illustrated in Fig. 20 in which the oxygen surface exchange coefficient k^q is plotted *vs.* electronic and ionic conductivities, respectively.

To summarize, the introduction of micro-ionic structures, *i.e.* thin film electrode structures with high reproducibility and fine geometrical control, has enabled a clear discrimination to be made between alternate rate limiting processes controlling the behavior of a model mixed ionic–electronic perovskite cathode material. The surface exchange reaction was shown conclusively to limit the overall cathodic oxygen reduction reaction. By examining the dependence of the oxygen exchange coefficient on Fe content in STF, it became clear that there is at best a weak dependence of k^q on the bulk electronic and ionic conductivities. This suggests the need for close examination of the surface chemistry and structure of electrodes to aid in establishing the features that are most critical towards achieving enhanced performance. Towards this objective, the challenge will be how to successfully apply high resolution surface analytical tools capable of operating under *in situ* conditions,

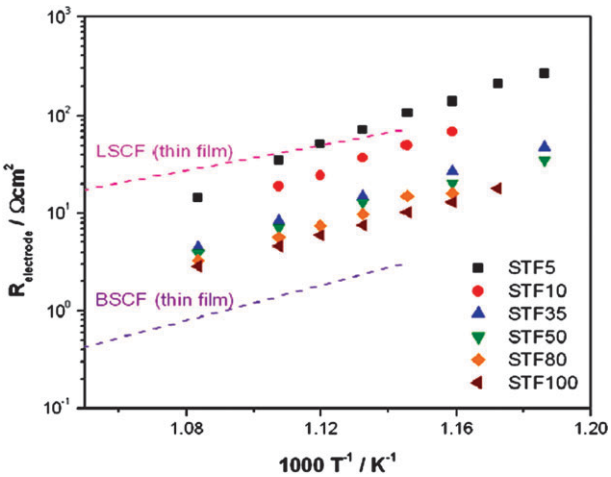

Fig. 19 The areal electrode resistance of a series of STF electrodes is plotted as a function of reciprocal temperature. Values for LSCF and BSCF from the literature[45] are included for comparison.

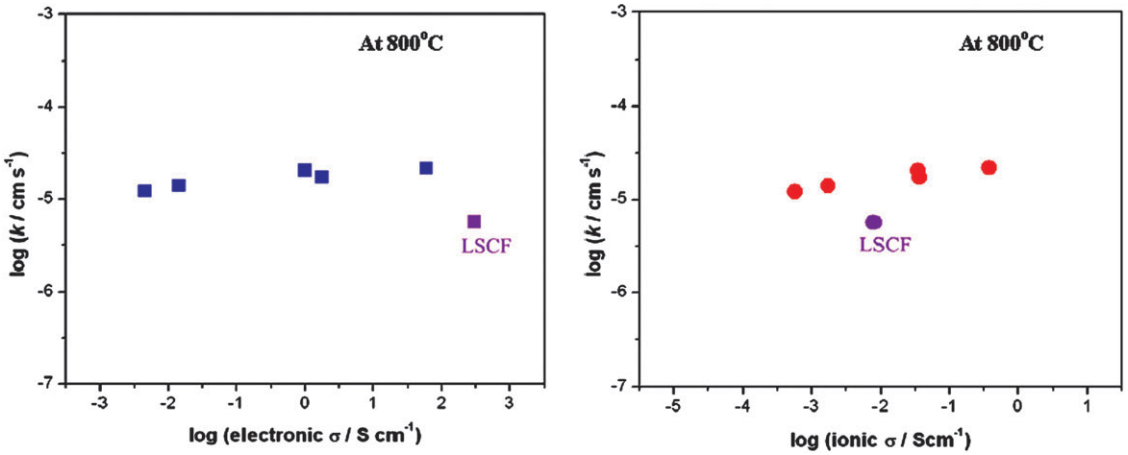

Fig. 20 The STF surface exchange coefficient measured at 800 °C as a function of the magnitude of electronic conductivity (left) and of ionic conductivity (right). Corresponding values for LSCF taken from the literature[48,49] are shown for comparison.

characterized by both elevated temperatures and a range of often reactive atmospheres.

Conclusions

The desire for ever smarter systems-on-a-chip and plug-free portable electronics with longer operating times between recharge has stimulated growing interest in micro-ionic systems. Given their small size and the need to often integrate such *micro-ionic* devices with corresponding *microelectronic* devices dictates the use of thin film and photolithographic processing techniques, commonly at temperatures considerably below those utilized in conventional ceramics processing methods. This leads to ionic or mixed ionic–electronic materials with nanosized dimensions. The implications for nanosized grains on the ionic conductivity of thin film solid oxide electrolytes were examined. Transport along and across grain boundaries can come to dominate the transport properties of such nano-dimensioned materials. The challenge is to learn how to perform *grain boundary engineering* as a means of controlling and ultimately enhancing such transport. Heterogeneous doping by selective in-diffusion along grain boundaries was introduced as a potentially powerful means of achieving this.[16] Progress along these lines will also be assisted by improving our means of modeling space charge distributions at such boundaries.[14,31,32] The clean room conditions used by the microelectronic industries also contribute to higher purity materials and interfaces and thereby offer improved reproducibility, lower defect densities and a heightened ability to isolate contaminants which contribute to degraded performance. Other approaches, borrowed from microelectronics, including the growth of heterojunction structures with well defined periodicity, can be expected to lead to improved and/or unexpected properties.[23,26,50,51] Likewise, the ability to create geometrically well defined structures by lithographic methods has already led to means for achieving a much improved understanding of electrode processes in SOFC structures.[41–44] Indeed, the more idealized structures achievable by application of microelectronic processing provide a marvelous opportunity to uncover the science underlying the technology of micro- and ultimately macro-ionics.

Acknowledgements

Funding for this research was provided by NSF (DMR-0243993) under a Materials World Network collaboration with Professors E. Ivers-Tiffee and D. Gerthsen, Univ. Karlsruhe and partial support for W. Jung *via* a Samsung Scholarship. RWTH Aachen University is gratefully acknowledged for providing a Charlemagne scholarship for a student visitation by S.J. Litzelman and thanks are due to Prof. M. Martin and Dr R. De Souza of RWTH Aachen University for their collaboration on the grain boundary diffusion studies. Helpful discussions with and assistance from previous group members including J. L. Hertz, A. Rothschild and K. Sahner are highly appreciated.

References

1 C. D. Baertsch, K. F. Jensen, J. L. Hertz, H. L. Tuller, S. T. Vengallatore, S. M. Spearing and M. A. Schmidt, *J. Mater. Res.*, 2004, **19**, 2604–2615.
2 D. Beckel, A. Bieberle-Hütter, A. Harvey, A. Infortuna, U. P. Müecke, M. Prestat, J. L. M. Rupp and L. J. Gauckler, *J. Power Sources*, 2007, **173**, 325–345.
3 C. K. Dyer, *Sci.Am.*, 1999, **281**, 88–93.
4 D. Nikbin, *Fuel Cell Rev.*, 2006, **3**, 21–24.
5 Z. P. Shao, S. M. Haile, J. Ahn, P. D. Ronney, Z. L. Zhan and S. A. Barnett, *Nature*, 2005, **435**, 795–798.
6 J. L. Hertz and H. L. Tuller, in *Microfabricated Power Generation Devices: Design and Technology*, ed. A. Mitsos and P. I. Barton, ISBN: 978-3-527-32081-3, in press, Wiley-VCH, p. 45.
7 T. Ishihara, H. Matsuda and Y. Takita, *J. Am. Chem. Soc.*, 1994, **116**, 3801–3803.
8 A. Bieberle-Hütter, D. Beckel, A. Infortuna, U. P. Muecke, J. L. M. Rupp, L. J. Gauckler, S. Rey-Mermet, P. Muralt, N. R. Bieri, N. Hotz, M. J. Stutz, D. Poulikakos, P. Heeb, P. Müller, A. Bernard, R. Gmür and T. Hocker, *J. Power Sources*, 2008, **177**, 123–130.
9 A. Bieberle-Hütter, J. L. Hertz and H. L. Tuller, *Acta Mater.*, 2008, **56**, 177–187.
10 H. Huang, M. Nakamura, P. C. Su, R. Fasching, Y. Saito and F. B. Prinz, *J. Electrochem. Soc.*, 2007, **154**, B20–B24.
11 B. C. H. Steele, *Solid State Ionics*, 2000, **129**, 95–110.

12 Y. M. Chiang, E. B. Lavik, I. Kosacki, H. L. Tuller and J. Y. Ying, *Appl. Phys. Lett*., 1996, **69**, 185–187.
13 Y. M. Chiang, E. B. Lavik, I. Kosacki, H. L. Tuller and J. Y. Ying, *J. Electroceram*., 1997, **1**, 7–14.
14 A. Tschöpe, *Solid State Ionics*, 2001, **139**, 267–280.
15 S. Kim and J. Maier, *J. Electrochem. Soc*., 2002, **149**, J73–J83.
16 S. J. Litzelman, R. A. D. Souza, B. Butz, H. L. Tuller, M. Martin and D. Gerthsen, *J. Electroceram*., 2008, DOI: 10.1007/s10832-10008-19445-y.
17 D. F. Evans and H. Wennerström, in *The Colloidal Domain*, Wiley-VCH, New York, 1999.
18 W. Schottky, *Z. Phys*., 1939, **113**, 367–414.
19 S. M. Sze, in *Semiconductor Devices*, Wiley & Sons, New York, 1985.
20 X. Guo and J. Maier, *J. Electrochem. Soc*., 2001, **148**, E121–E126.
21 A. Tschope and R. Birringer, *J. Electroceram*., 2001, **7**, 169–177.
22 C. C. Liang, *J. Electrochem. Soc*., 1973, **120**, 1289–1292.
23 N. Sata, K. Eberman, K. Eberl and J. Maier, *Nature*, 2000, **408**, 946–949.
24 C. Wagner, *J. Phys. Chem. Solids*, 1972, **33**, 1051–1059.
25 J. Maier, *Prog. Solid State Chem*., 1995, **23**, 171–263.
26 J. Garcia-Barriocanal, A. Rivera-Calzada, M. Varela, Z. Sefrioui, E. Iborra, C. Leon, S. J. Pennycook and J. Santamaria, *Science*, 2008, **321**, 676–680.
27 I. Kaur, Y. Mishin and W. Gust, in *Fundamentals of Grain and Interphase Boundary Diffusion*, Wiley & Sons, West Sussex, 1995.
28 L. G. Harrison, *Trans. Faraday Soc*., 1961, **57**, 1191–1199.
29 S. J. Litzelman and H. L. Tuller, *Solid State Ionics*, 2008, submitted.
30 I. Riess, *Solid State Ionics*, 1996, **91**, 221–232.
31 J. Maier, *Ber. Bunsen-Ges*., 1986, **90**, 26–33.
32 S. J. Litzelman, PhD thesis, Massachusetts Institute of Technology, 2008.
33 O. Yamamoto, Y. Takeda, R. Kanno and M. Noda, *Solid State Ionics*, 1987, **22**, 241–246.
34 S. B. Adler, *Chem. Rev*., 2004, **104**, 4791–4843.
35 G. W. Coffey, L. R. Pederson and P. C. Rieke, *J. Electrochem. Soc*., 2003, **150**, A1139–A1151.
36 M. Liu, *J. Electrochem. Soc*., 1998, **145**, 142–154.
37 M. Prestat, J. F. Koenig and L. J. Gauckler, *J. Electroceram*., 2007, **18**, 87–101.
38 L. H. Brixner, *Mater. Res. Bull*., 1968, **3**, 299–308.
39 A. Rothschild, W. Menesklou, H. L. Tuller and E. Ivers-Tiffée, *Chem. Mater*., 2006, **18**, 3651–3659.
40 W. Jung and H. L. Tuller, *J. Electrochem. Soc*., 2008, **155**, B1194–B1201.
41 F. S. Baumann, J. Fleig, H. U. Habermeier and J. Maier, *Solid State Ionics*, 2006, **177**, 1071–1081.
42 A. Bieberle, L. P. Meier and L. J. Gauckler, *J. Electrochem. Soc*., 2001, **148**, A646–A656.
43 J. L. Hertz and H. L. Tuller, *J. Electroceram*., 2004, **13**, 663–668.
44 Y. L. Yang, C. L. Chen, S. Y. Chen, C. W. Chu and A. J. Jacobson, *J. Electrochem. Soc*., 2000, **147**, 4001–4007.
45 F. S. Baumann, J. Fleig, G. Cristiani, B. Stuhlhofer, H. U. Habermeier and J. Maier, *J. Electrochem. Soc*., 2007, **154**, B931–B941.
46 J. Fleig, *J. Power Sources*, 2002, **105**, 228–238.
47 J. Maier, *Physical Chemistry of Ionic Materials: Ions and Electrons in Solids*, John Wiley & Sons Ltd, West Sussex, 2004.
48 S. J. Benson, R. J. Chater and J. A. Kilner, *Proceedings of the 3rd International Symposium on Ionic and Mixed Conducting Ceramics, Proceedings Volume 97-24*, ed. T. A. Ramanarayanan, W. L. Worrell, H. L. Tuller, A.C. Khandkar, M. Mogensen and W. Gopel, The Electrochemical Society, Pennington, NJ, 1997, pp. 596–609.
49 H. Ullmann, N. Trofimenko, F. Tietz, D. Stover and A. Ahmad-Khanlou, *Solid State Ionics*, 2000, **138**, 79–90.
50 S. Azad, O. A. Marina, C. M. Wang, L. Saraf, V. Shutthanandan, D. E. McCready, A. El-Azab, J. E. Jaffe, M. H. Engelhard, C. H. F. Peden and S. Thevuthasan, *Appl. Phys. Lett*., 2005, **86**, 131906–131903.
51 W. Jung, J. L. Hertz and H. L. Tuller, *Acta Mater*., 2009, DOI: 10.1016/j.actamat.2008.11.028.

